Mechanisms of gas and shrinkage porosity formation in solidifying shear bands

Shishira Bhagavath[1,2,+], Zhixuan Gong[2,3,+], Tim Wigger[2,3], Saurabh Shah[2,3], Bita Ghaffari[4], Mei Li[4], Shashidhara Marathe[5], Shyamprasad Karagadde[1,#], Peter D Lee[2,3,#]

[1] University College London, London WC1E 6BT, UK

[2] Research Complex at Harwell, Harwell Campus, OX11 0FA UK,

[3] Department of Mechanical Engineering, Indian Institute of Technology Bombay, Mumbai 400076, India

[4] Ford Research and Advanced Engineering, Dearborn, USA

[5] Diamond Light Source, Harwell Campus, OX11 0DE, UK

[+] Equal contribution

[#] Corresponding authors: s.karagadde@iitb.ac.in , peter.lee@ucl.ac.uk

Abstract

In specialised solidification processing techniques such as High Pressure Die Casting, twin-roll casting and others, an additional external deformation load is applied to achieve the required shape, leading to the formation of microstructural features such as shear bands. The mechanism for forming these features is believed to be dependent on dynamically evolving strain fields, which are dependent on the local solid fraction, applied strain rates and casting geometry. To investigate this, a semisolid (~50% solid fraction) Al-10 wt.% Cu alloy is isothermally injected into a bespoke die using a custom-designed thermo-mechanical rig. The semisolid deformation, formation of Cu-rich dilatant bands and subsequent pore nucleation and growth are captured using fast synchrotron X-ray radiography. The local normal and shear strains acting on the mush are quantified using Digital Image Correlation to identify the dilatant shear bands and the dominant local strain component. Correlating the radiographs with strain maps reveals that gas pores within the dilated interstices grow, while those in compressed regions are squeezed out. A linear correlation between accumulated volumetric strain and porosity volume fraction demonstrates that higher dilations give rise to a local increase in both gas and shrinkage porosity.

Keywords: Semisolid; Dilatancy; X-ray radiography; Digital image correlation; Gas porosity

1. Introduction

Externally imposed deformation is employed in many metal casting processes such as High Pressure Die Casting (HPDC), twin-roll casting and others, achieving net-shape geometry while increasing the casting quality. Among these, HPDC is a widely used manufacturing process, in which an additional pressure of up to 120 MPa and an injection velocity of 30-60 m/s is applied during the injection, and intensification stages whilst the metal solidifies. However, a large number of defects can occur in finished HPDC castings, such as shear bands, porosity, externally solidified crystals (ESC) and cracks. Bonollo et al. (2015) in their survey on European foundries found that 35% of all HPDC casting defects are related to porosity, which constitute a significant cause for HPDC component failure.

Various studies have been reported on the effect of porosity on the strength and fatigue properties of HPDC components. Cao and Wessén (2005) reported two kinds of defect bands based on pre-solidified crystals and found that porosity and eutectic segregation in bands decreased significantly with increasing intensifying pressure. Otarawanna et al. (2010) studied the effect of intensifying pressure on HPDC porosity and reported the formation of the shear band through the gate at higher intensifying pressures. Outmani et al. (2017) studied the effect of intensifying pressures on reducing the gas and shrinkage porosity. However they did not report on the effect of intensification on porosity banding. Li et al. (2016) used X-ray tomography to study the porosity defect in HPDC and reported four porosity types: gas, gas shrinkage, and total and island shrinkage pores. Li et al. (2017) further investigated the influence of melt flow and ESCs on the formation of defect bands near the gate in AZ91D magnesium alloy. They found that the defect bands concentrated along the cross-section where the gate region opens to a larger die. Recently, Yu et al. (2021) characterised the porosity band using X-ray tomography and reported that the tensile cracks propagated through the defect bands containing accumulated ESCs and shrinkage pores. Since such defects have detrimental effects on cast components strength and fatigue resistance, understanding the deformation behaviour in the semisolid state is critical for manufacturers. In this regard, several semisolid tensile, compression, and shear tests have been performed, and a detailed review of these experiments was reported by Eskin et al. (2004).

The semisolid state is conventionally considered as a continuous visco-plastic system, in which the compaction of the solid network accommodates the externally imposed stress, and the intergranular liquid is squeezed out. Martin et al. (1997) proposed constitutive visco-plastic equations for a porous medium of growing solids. This is followed by a strain rate dependent visco-plastic model developed by Zavaliangos (1998), which capture the microstructural mechanisms during semisolid compression at higher solid fractions. Based on the observations and studies originating from the field of soil mechanics, the granular theory of dilatancy was later proposed to explain localised features such as eutectic bands and porosity, notably by Tzimas and Zavaliangos (1999). They investigated the strain localisation phenomena and attributed the banding to the destruction of cohesion between grains and increased volumetric strain due to dilatancy. Dilatancy describes the phenomenon of grain rearrangement, leading to an increase in intergranular space and liquid segregation to fill these spaces. The mechanisms can be distinguished by considering the material as either a continuum bulk structure where compaction occurs, or as an assembly of cohesionless grains leading to dilatancy. Gourlay and Dahle (2007) suggested that this competition is critically dependent on the grain size, morphology, fraction solid, and the corresponding grain cohesion.

In the past two decades, a large number of *in situ* synchrotron deformation studies on semisolid metallic systems have provided direct evidence of the granular mechanisms. Real-time tomography (4D) experiments performed by Kareh et al. 2014 revealed the granular mechanics on a cylindrical specimen in the semisolid state under compression and quantified the effect of dilation on the crack formation and liquid segregation by measuring the evolving volumetric strain. Similar experiments were performed by Cai et al. (2014), who proposed a mechanism for rapid growth of dilatancy induced shrinkage pore. However, these experiments were performed at slow deformation rates (~5-10 μm/s) to avoid motion blur artefacts. Using radiography on thin sections, shear-induced dilation was confirmed in semisolid aluminium alloys by Gourlay et al. (2011) and in carbon steel alloys at higher solid fractions by Kareh et al. (2017). More recently, a quantitative analysis of the granular mechanics was presented by developing a Discrete Element Method model by Su et al. (2019). Furthering on their work, Su et al. (2020) modelled the transition from suspension to granular flows using a coupled Lattice Boltzmann method-

Discrete Element Method model and radiography experiments. The model demonstrated how the shear cracks are developed from dilatancy-induced pressure drop. They showed the drop in local liquid pressure due to dilatancy, which corresponds to the first location of the cracking.

Most of the prior literature describes the granular mechanics, shear cracking and subsequentially the liquid segregation. However, the quantification of the final porosity is limited with respect to the type of deformation. Several prior *in situ* experiments were performed on samples with a uniform cross-section. Thus, the role of a varying cross-section needs to be investigated, which not only impacts the local cooling and microstructures but also provides considerably different strain fields in the same plane. To overcome these gaps, fast *in situ* synchrotron X-ray radiography experiments using a lab-scale pressurised casting system were performed. A partially solidified Al-Cu alloy was injected into a thin flat mould using a specially designed thermomechanical rig. The two-dimensional X-ray image datasets were quantified by digital image correlation (DIC), obtaining full-field strain maps throughout the deformation process. The fast radiography imaging technique also permitted capturing the behaviour of gas bubbles in the dilation banding regions. Moreover, the final porosity is correlated with the local volumetric strain during the deformation. A statistical description of the porosity volume fraction against the integrated volumetric change is proposed, providing a quantitative basis for the development of porosity prediction models for pressurised casting.

2. Methods

2.1 Experimental setup and materials

An Al-10 wt.% Cu alloy (referred to as Al-10Cu henceforth) was selected as sample material due to the enhanced X-ray image contrast between the primary aluminium phase and the Cu-rich eutectic liquid. The desired fraction solid was ascertained by controlling the temperature as estimated by the Scheil solidification module of ThermoCalc®, a commercial Calphad tool by Andersson et al. (2002).

A custom-designed, lab-scale die-piston assembly was placed in a furnace with resistive heating and integrated into a bespoke mechanical loading rig (P2R) (Fig.1). As shown in Fig.1(a), a rectangular, 11 mm wide × 10 mm tall × 1 mm thick specimen was inserted into an alumina piston attached to the bottom ram of the mechanical rig, with a matching inside slot of 1 mm width. The samples were manufactured by Electrical Discharge Machining as flat rectangular samples of 11×12 mm^2 cross section and 1 mm thickness. To remove any potential high-stress concentration points, the edges were slightly rounded using 320 grit SiC emery sheets. The sample edges were carefully tapered for the samples to fit smoothly inside the hollow piston. They were placed inside so that the top surface of the sample is completely inside the piston, with sideways movement minimised. To observe the effect of the cross-sectional change on local defect formation, an alumina die with a 'T-shaped' cavity was placed on top, fitting tightly inside the piston. The die was held by the upper and bottom rams of the P2R rig, enabling movement along the vertical direction to apply pressure. The displacement and load precisions were 100 nm and 0.1 N, respectively.

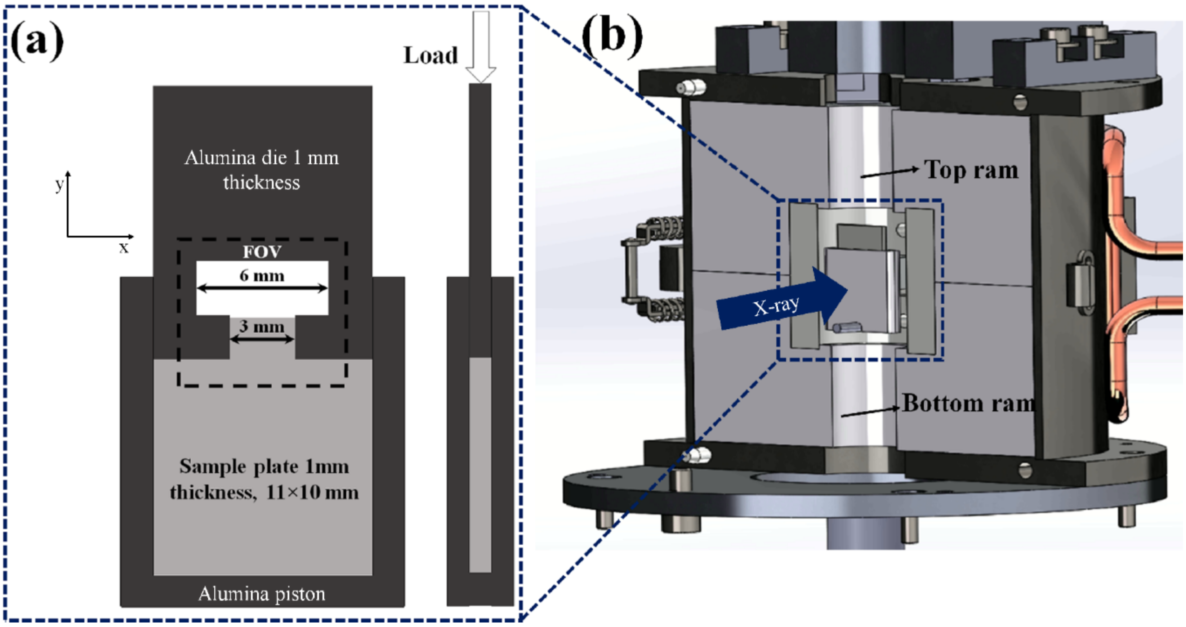

Fig.1. Experimental setup used in I13-2 beamline: (a) Cross-sectional view and side view of the assembly showing the main components of the sample holder (b) Sample holder stage and the Laura PID resistance furnace mounted on the P2R mechanical rig.

2.2 Experimental procedure

The experiments were carried out on the I13-2 beamline at Diamond Light Source, UK (beamtime reference MG22053-1). A pink X-ray beam with a photon energy of 27 keV passed through X-ray transparent windows in the furnace, penetrated the specimen and was captured using module 1 of a PCO Edge 5.5 high-speed camera. The imaging field of view was 6.7 mm × 5.6 mm, with an average pixel size of 2.6 μm.

The specimens were heated to achieve 50% fraction solid and isothermally held for 10 min to homogenise. The die was then pushed downwards at a rate of 80 μm/s, and thus the melt was injected into the T-shaped cavity due to backward extrusion. The image acquisition was initiated when the injection started, and 6000 images were continuously captured over ~60 s deformation time. To quantitatively analyse the defects in 3D, the cast samples were afterwards analysed *ex situ* by high-resolution micro–Computed Tomography (μCT) (Nikon XTH, 225, UCL Centre for Correlative X-ray Microscopy). For each tomogram, 3185 projections were taken at an effective pixel size of 7.96 μm.

2.3 Image processing and quantification

The radiography datasets were processed with Fiji ImageJ, an open-source image processing software developed by Schindelin et al. (2012) (US NIH, Bethesda, MD, USA) and MATLAB2015b (Mathworks Inc., USA). The flat-field correction was applied as the initial step. The background, obtained by averaging the image stacks, was subtracted from the entire set of radiographs to remove the background noise and blemishes on the ceramic piston.

Digital image correlation (DIC) analysis was applied on the radiographical datasets using an open-source MATLAB algorithm, Ncorr developed by Blaber et al. 2015. To enhance the contrast, the images were filtered using a Fast Fourier Transform (FFT) bandpass filter with a size of 40 pixels. The filtered image frames and the tracked intensity features are shown in Supplementary Fig. S1. Subsequently, circular subsets with a radius of 40 pixels were selected as a trade-off between the correlation coefficient and spatial resolution of strain calculation. Three-component accumulated strain maps (horizontal, vertical and shear) were obtained throughout the deformation process. The volumetric strain is given by:

$$\frac{\Delta V}{V} = \varepsilon_{xx} + \varepsilon_{yy} + \varepsilon_{xx} \times \varepsilon_{yy} \qquad \text{Equation (1)}$$

where ε_{xx} and ε_{yy} are the normal strains. By making the small strain approximation, the product of the normal strains can be ignored. Thus, the volumetric strain is estimated as a sum of normal strain components:

$$\frac{\Delta V}{V} = \varepsilon_{xx} + \varepsilon_{yy} \qquad \text{Equation (2)}$$

The tomograms obtained by *ex situ* scans were reconstructed using a filtered back-projection algorithm and processed using Avizo 9.1 (Thermo Fisher Inc). Supplementary Fig. S2 shows an individual XY tomogram slice, where the primary phase (aluminium dendrites) are dark grey, the eutectic liquid (Cu-enriched) is light grey, and the pores appear black. Please note that in Fig. S2, the radiography images, features that are lighter grey appear darker in tomography slices. The remaining features, such as the alumina die and the background, were masked out. Smaller voids (<50 voxel) and sample edges were neglected in the analysis. The pores were segmented using a global greyscale threshold.

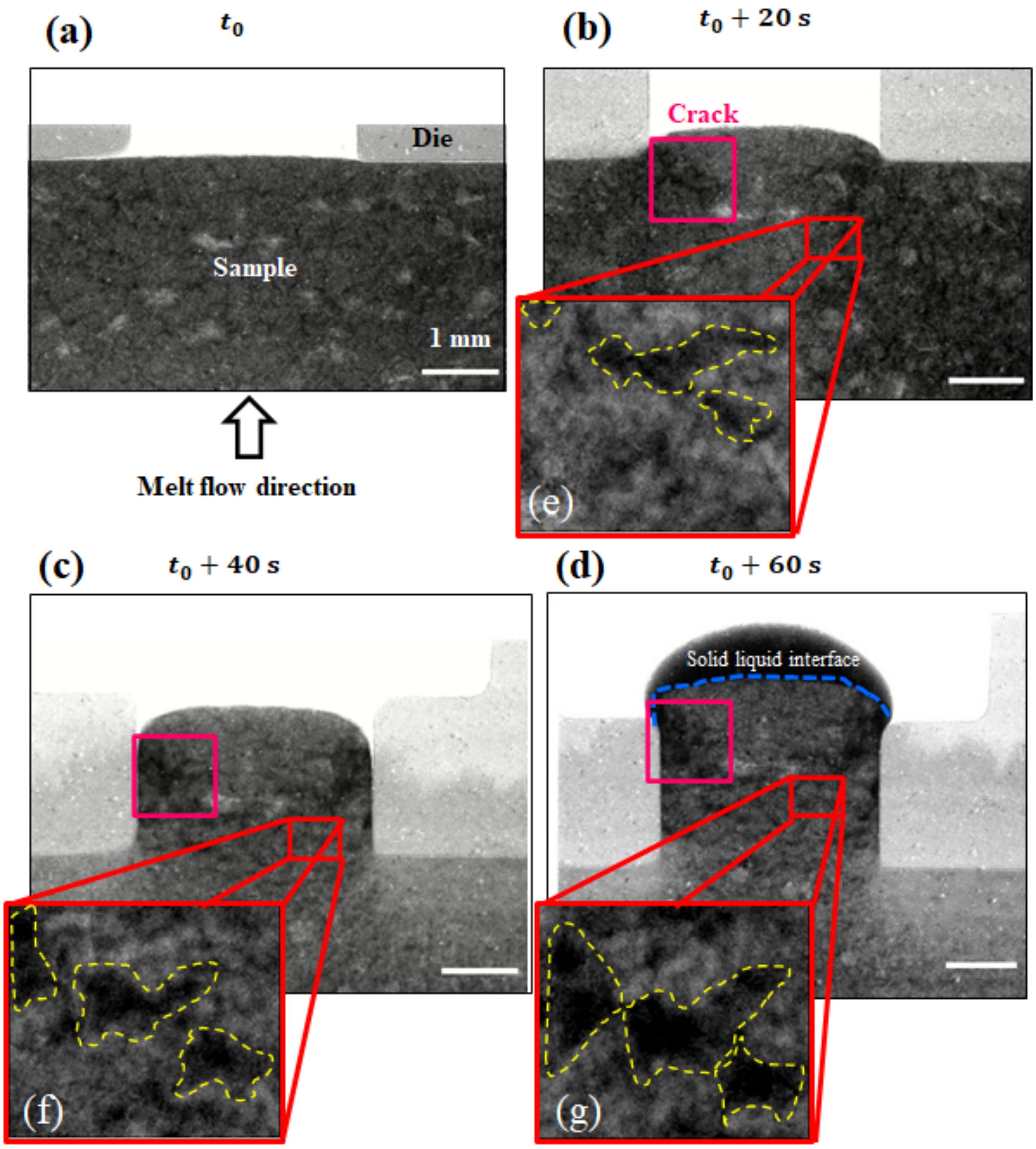

Fig.2. X-ray radiographical image sequence showing the injection process (t_0 is at the beginning of loading): (a-d) The injection process from t_0 to t_0 +60 seconds. Note that darker grey indicates the inter-dendritic liquid (Cu-rich), medium grey represents the solid dendritic networks. (See Supplementary Video 1); (e-g) Zoomed-in images show the evolution of the intergranular shear band forming during the injection.

3. Results

3.1 Shear-induced dilation in extrusion region

Fig. 2(a-d) show the injection of an Al-10Cu sample at a global solid fraction of 50%. Before the injection (Fig. 2(a)), the grains and inter-dendritic liquid appear as a homogeneous mixture without any noticeable segregation. As the sample is injected, the greyscale intensity of the region below the die (symmetrical, on both the left and right sides) becomes lighter, whilst the intensity at the central inlet gets darker, indicating a local redistribution of the solid. Fig. 2(e-g) show the magnified view of the region where these changes are observed, where the yellow dashed lines outline the intergranular gaps, into which the Cu-rich liquid has flown. In the early stages of deformation, the gaps are thin, but with the increased strain, they are stretched along the vertical loading direction and merge, forming a band. These bands are a characteristic feature seen in commercially produced HPDC components. A liquid-filled crack at the solid-liquid interface (outlined in the purple box in Fig. 2(b-d)) do not show significant morphological change after entering the narrow region of the T section ($t > 20$ s).

The strain maps are obtained using DIC, to gain insights into the strain state of the sample in critical regions. Three strain components (shear, vertical and horizontal) at different time steps (33.8 s, 36.8 s and 39.8 s after the start of loading) are shown in Fig. 3, indicating the strain evolution. For normal strains, positive values indicate tensile strain (shown in red), while negative values represent compressive strain (shown in blue). The mirrored halves of the radiography images displayed on the left side of each panel show the corresponding radiographs. Based on the dominant strain components, three distinct regions were defined as I - Dilation region, II - Compaction region, and III - Intermediate region, as indicated in Fig. 4.

In region I, the mush predominantly undergoes tension in the y-direction (refer to Fig. 1), which is consistent with the formation of the growth of the intergranular gap shown in Fig. 2(g-i). The liquid segregation is possibly caused by dilation-assisted feeding and bulk flow feeding on other regions, as seen by the shear localisation along the alumina die wall in Fig. 3. The mush is under direct compaction load in region II, as indicated by the vertical compressive strains shown in Fig. 3(g-i). The corresponding microstructure on the left shows densely compacted solid grains and significantly increased local solid fraction. In region III, since the solid networks have largely accommodated the applied load in region II, the solid phase in this area needs to withstand reduced compression stress. Additionally, unlike region I, region II does not exhibit dilation as it is further away from the edges where large shear persists. The microstructure almost remains the same as before injection, and the measured normal strain is less than 0.1.

3.2 Deformation-induced pore formation

The mechanism of void formation is attributed to the failure of the inter-dendritic liquid to sufficiently compensate for the opening of solid network. In this experiment, openings in the solid networks are fed by bulk liquid flow. This Cu-rich liquid is the last solidifying region due to its lower melting temperature and also the location of shrinkage porosity. In region I, a less-reported phenomenon of deformation-induced gas bubble growth is observed. While the semisolid sample is isothermally held before the injection, some gas bubbles are generated in the liquid. These bubbles are observed to be entrapped in the solid dendrite network. Fig. 4(a-c) show an example of a bubble (A) observed in the region I. The bubble morphology initially appears to be elliptical. The gas pore grows further controlled by diffusion, where the flux for the growth is provided by hydrogen convection through the bulk liquid flow. The equivalent radius of the bubble (A) increases from 35 μm to 70 μm in 7 seconds and shrinks thereafter. The reduction in size is attributed to the change in local curvatures. Sun et al., 2018 observed such a decrease in pore size due to the impingement of Al-Ni intermetallics using in situ radiographic experiments. They attributed the reduction in size due to the negative flux from the pore-liquid surface due to a change in local curvature. Due to the impingement of solids, the local curvature changes, resulting in a negative concentration gradient at the interface. This leads to a negative growth velocity, i.e., a reduction in pore size. The maximum shear strain at the corresponding time is plotted, demonstrating an ongoing deformation during this period.

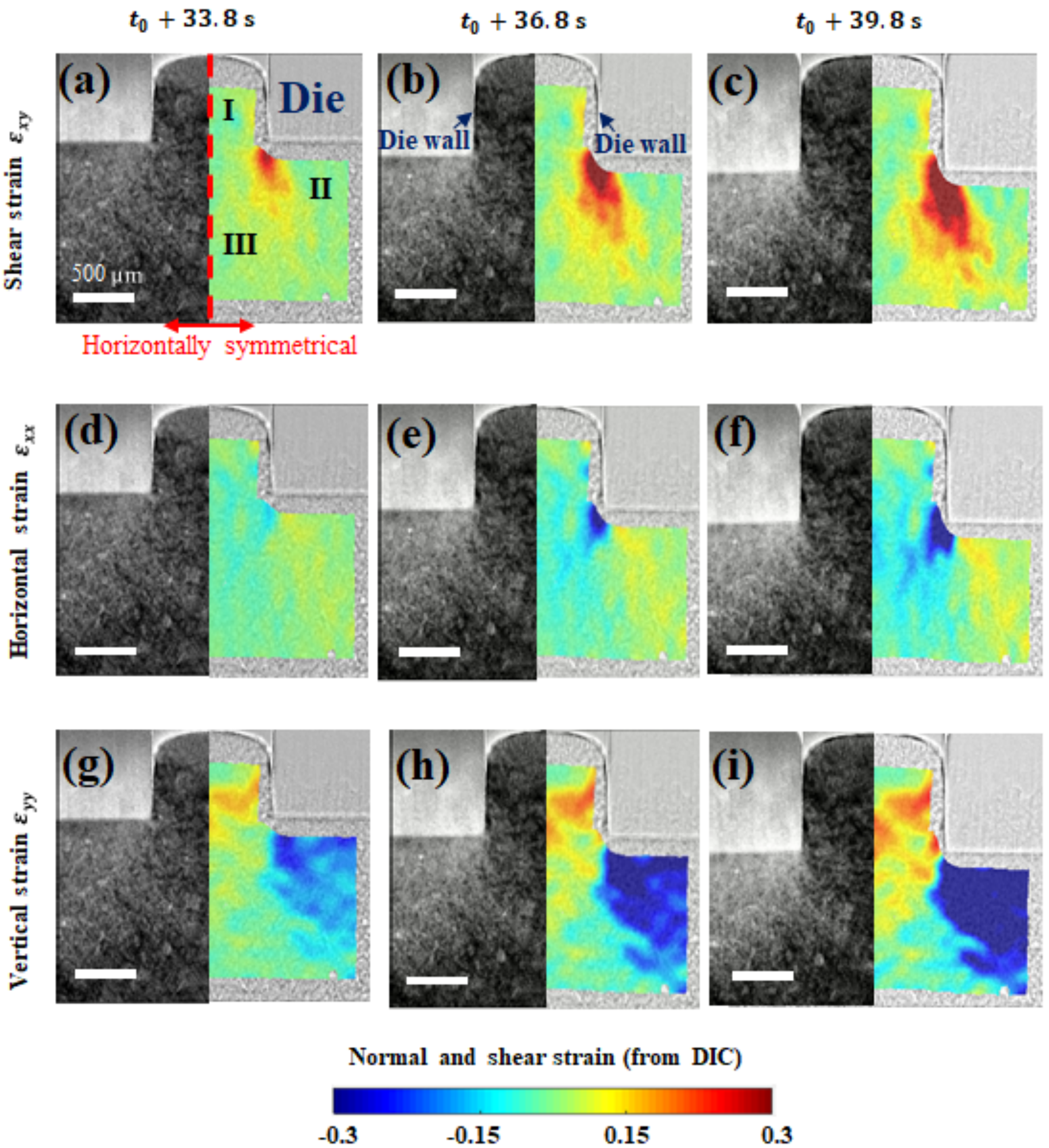

Fig.3. Analysis of radiographic X-ray images using DIC: Processed images showing the local dendrite network distribution change from 33.8 s to 39.8 s after deformation are shown on the left of each panel, and (a-c) corresponding shear strain; (e-f) Horizontal strain; (g-i) Vertical strain evolution are on the right side.

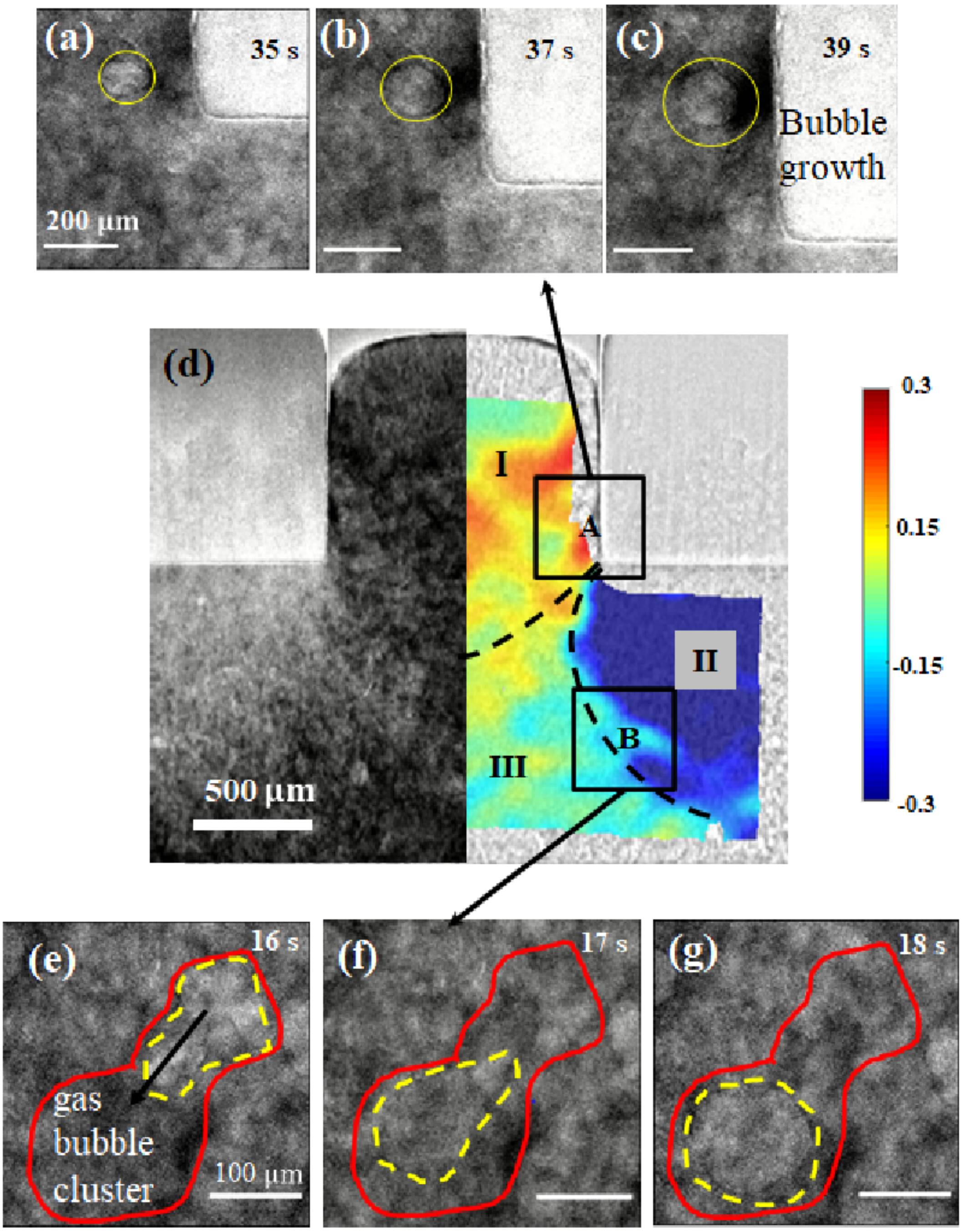

Fig.4. Radiographs capturing the gas bubble behaviour: (a-c) Magnified figures showing bubble growth in the dilation region (see Supplementary Video 2); (d) DIC measurement indicating the localised strain in: I dilation region, II contraction region and III transition region, which is characterised by least deformation; (e)-(g) Enlarged figure indicating a cluster of gas bubbles migrating from high-pressure region to low-pressure region (Supplementary Video 3).

Fig. 4(e-g) show bubble (B) shifting from region II to region III through the grain interstices in 2 seconds, regenerating as a single round bubble. The behaviour of the bubble growth can be explained by considering an Ostwald-type growth mechanism. This type of coarsening mechanism was observed and modelled in Berca sandstone, which was used to store CO_2 by De Chalendar et al., (2018). We observe that the local ambient pressure plays a role in determining the growth mechanism. The higher compressive strain in region II, as seen in the DIC measurements, forces the bubble into region III.

4. Discussion

The results clearly show the response of the semisolid region to deformation in a varying cross section. The observations suggest that a dilated region forms adjacent to the locations of high shear stress. A schematic of the mechanisms of banding and resulting pore formation is shown in Fig. 5.

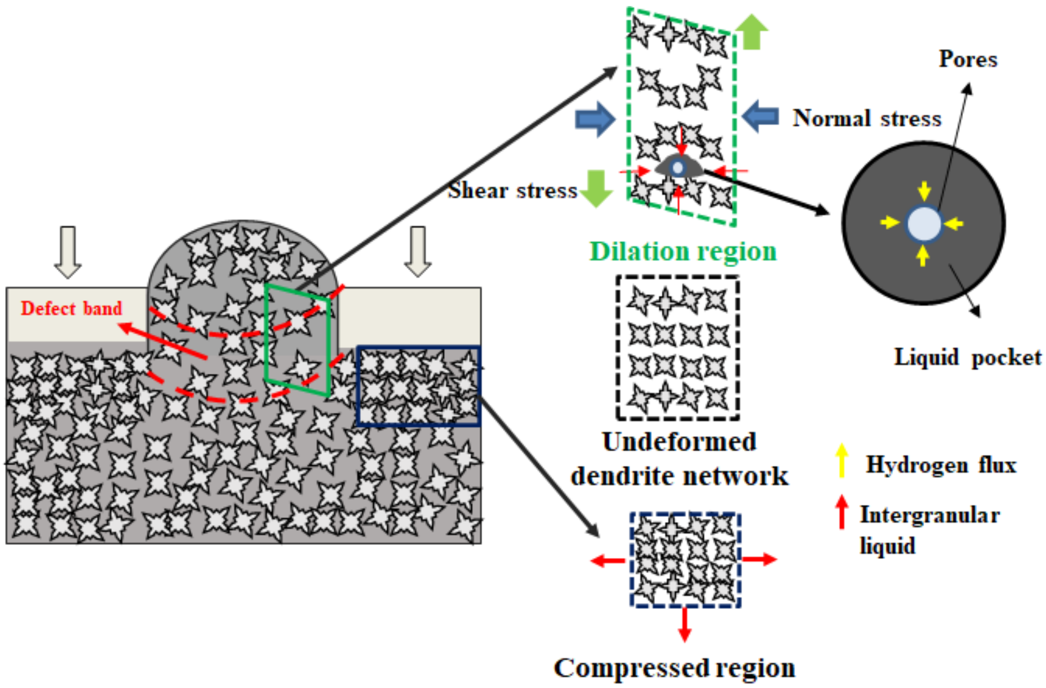

Fig.5. A schematic of mechanism illustrating the strain evolution in the region under high shear strain and the region under compression leading to liquid and solid redistribution.

Upon continued deformation, the inter-dendritic gaps open, and the solute-enriched liquid is drawn into the gap, which has a larger propensity in nucleating gas pores due to further influx of the dissolved hydrogen from the nearby regions. Sistaninia et al. (2013) showed that a large pressure drop from the bulk liquid and the mushy zone using a three-phase coupled finite element, semisolid deformation and failure modules. The lower pressure in the dilated band also means that the diffusion gradients and bubble growth rates can be more prominent owing to a reduced interface concentration given by Seivert's law. Further, the region around such bubbles undergoes reduced heat transfer (acting as a hot spot) as reported by Lee and Gokhale, (2006), and eventually, feeding (and hydrogen influx thereof) is restricted. This restriction leads to an accelerated pore growth as observed in situ during semisolid compression by Bhagavath et al. (2019) for MADC12 alloy and Cai et al. (2014) for Al-Cu binary alloy. This causes shrinkage effects to dominate and further increases the porosity.

4.1 Volumetric strain measurement and strain-porosity correlation

Based on the aforementioned mechanism, the dependency of the porosity on the volumetric strain can be investigated by quantifying it along several dilated regions. Using DIC and tomographic slices, the volumetric dilation behaviour is quantitatively correlated to the final porosity formation in a particular region of interest, as shown in Fig. 6. A 2D view of the reconstructed tomogram obtained post-mortem is shown in the inserted image in Fig. 6(a). Region I is evenly divided into six zones along the vertical direction shown as black boxes. The pores were segmented using a greyscale threshold and are shown in blue. The average volume fraction of the pores in each zone is measured. By utilising the distance of each zone to the melt front to track the zones, the accumulated volumetric strains in the same area are measured by DIC from radiography datasets throughout the deformation. Fig. 6(a) shows that a higher dilation strain leads to increased porosity formation, and the region under contraction contains the lowest pore volume. Furthermore, the porosity fraction changes as a function of volumetric strain as shown in Fig. 6(b). The high concentration of Cu-enriched liquid in the dilated regions can enable remelting of the surrounding dendrites, which further increases the local liquid fraction in the dilatant bands. The result is a higher final pore volume and hence a deviation from the linear trend.

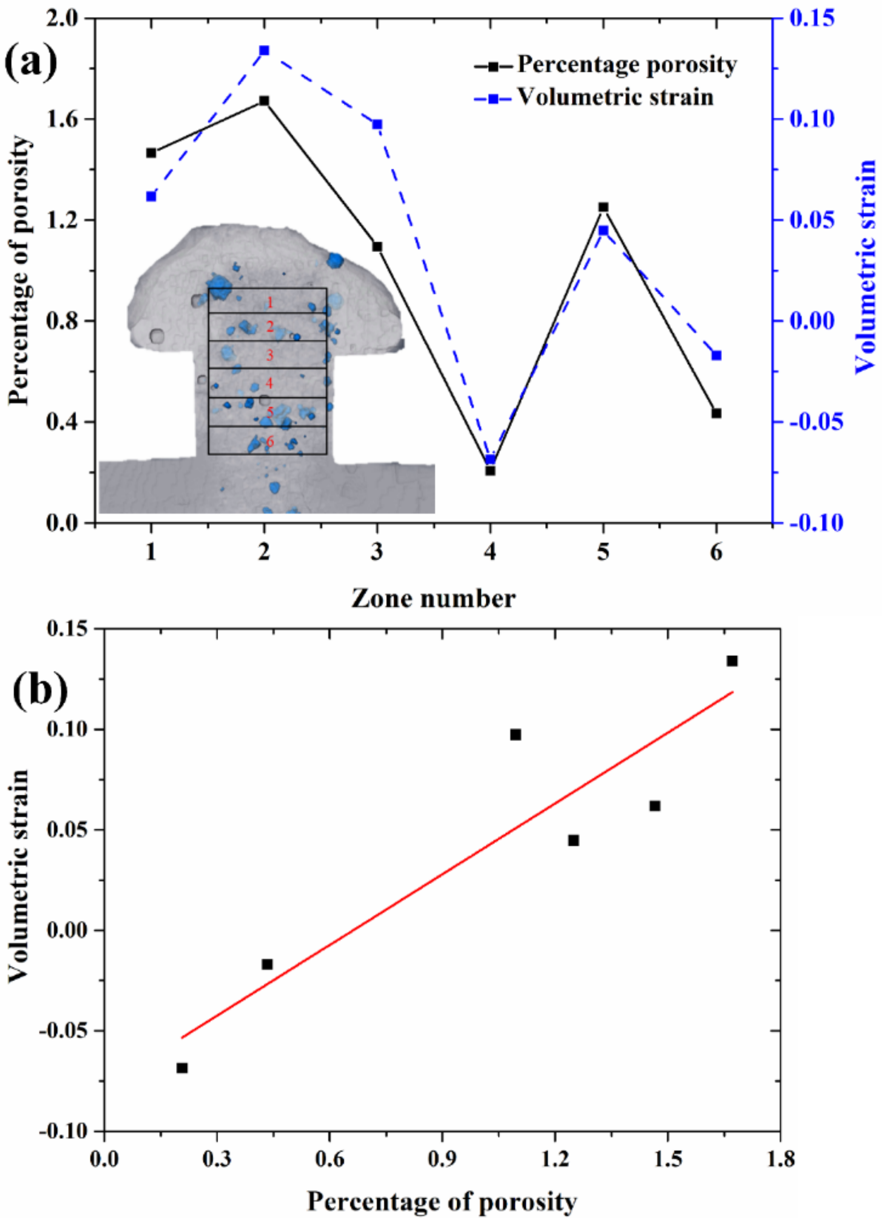

Fig. 6. Quantification of porosity and accumulated volumetric strain at different heights along the injection path: (a) Variation in shrinkage and gas porosity along with the volumetric strain corresponding to the six zones outlined

in the inset; (b) A linear correlation between the volumetric strain and percentage of porosity was observed in the six zones, clearly indicating that dilated shear bands are likely to have porosity in castings.

5. Conclusion

Fast synchrotron X-ray radiography was used to qualitatively and quantitatively analyse the injection of Al-10Cu into a T-shaped cavity, to investigate the effect of varying die cross sections, a typical feature of manufactured parts. The results revealed and confirmed the mechanisms of shear band formation and associated dilatancy. The analysis of full-field strain evolution using DIC shows regions of high strain concentrations with different dominating strain components. Three distinct regions of strain evolution were identified: I. shear dilation region, where the intergranular interstices open up, forming the liquid segregation band; II. compression region, where the solid dendrites are densely compacted, and the liquid within it is squeezed out; and III. intermediate region, where the microstructure is retained due to the minimal stress applied. These mechanisms significantly affect the porosity formation by altering local liquid/solid fraction and directly leading to gas bubble growth and migration. The percentage of porosity was found to increase by a factor of nine when the average volumetric strain increased from -0.075 in compression to 0.15 in tension. The accumulated volumetric strain is directly linked to the final percentage of porosity, demonstrating that higher volumetric strain leads to higher porosity.

Acknowledgements:

PDL and SK acknowledge the University Research Program at Ford Motor Company, USA for partial financial support and sanctioning the project P1299 under the SPARC (Scheme for Promotion of Academic and Research Collaboration) initiative. We are grateful to Diamond Light Source for granting the beamtime (MG22053-1). We acknowledge the assistance of Sebastian Marussi in designing the ceramic die-piston arrangement and setting up the rigs for beamtime. The assistance from GS Abhishek and D Rees during the beamtime is deeply appreciated. This work was supported by the Royal Academy of Engineering (CiET1819/10) and Laboratory space and facilities were provided by the Research Complex at Harwell (funded in part through UK-EPSRC grant EP/P006566/1).

References

Bhagavath, S., Cai, B., Atwood, R., Li, M., Ghaffari, B., Lee, P.D., Karagadde, S., 2019. Combined Deformation and Solidification-Driven Porosity Formation in Aluminum Alloys. Metall. Mater. Trans. A Phys. Metall. Mater. Sci. 50, 4891–4899. https://doi.org/10.1007/s11661-019-05378-8

Blaber, J., Adair, B., Antoniou, A., 2015. Ncorr: Open-Source 2D Digital Image Correlation Matlab Software. Exp. Mech. 55, 1105–1122. https://doi.org/10.1007/s11340-015-0009-1

Bonollo, F., Gramegna, N., Timelli, G., 2015. High-pressure die-casting: Contradictions and challenges. Jom 67, 901–908. https://doi.org/10.1007/s11837-015-1333-8

Cai, B., Karagadde, S., Yuan, L., Marrow, T.J., Connolley, T., Lee, P.D., 2014. In situ synchrotron tomographic quantification of granular and intragranular deformation during semi-solid compression of an equiaxed dendritic Al-Cu alloy. Acta Mater. 76, 371–380. https://doi.org/10.1016/j.actamat.2014.05.035

Cao, H., Wessén, M., 2005. Characteristics of microstructure and banded defects in die cast AM50 magnesium components. Int. J. Cast Met. Res. 18, 377–384. https://doi.org/10.1179/136404605225023216

De Chalendar, J.A., Garing, C., Benson, S.M., 2018. Pore-scale modelling of Ostwald ripening. J. Fluid Mech. 835, 363–392. https://doi.org/10.1017/jfm.2017.720

Eskin, D.G., Suyitno, Katgerman, L., 2004. Mechanical properties in the semi-solid state and hot tearing of aluminium alloys. Prog. Mater. Sci. 49, 629–711. https://doi.org/10.1016/S0079-6425(03)00037-9

Gourlay, C.M., Dahle, A.K., 2007. Dilatant shear bands in solidifying metals. Nature 445, 70–73. https://doi.org/10.1038/nature05426

J-O Andersson, Thomas Helander, Lars Hdghmd, Pingfang Shi, B.S., 2002. THERMO-CALC & DICTRA, Computational Tools For Materials Science. Calphad Comput. Coupling Phase Diagrams Thermochem. 26, 273–312.

Kareh, K.M., Lee, P.D., Atwood, R.C., Connolley, T., Gourlay, C.M., 2014. Revealing the micromechanisms behind semi-solid metal deformation with time-resolved X-ray tomography. Nat Commun 5, 4464. https://doi.org/10.1038/ncomms5464

Kareh, K.M., O'Sullivan, C., Nagira, T., Yasuda, H., Gourlay, C.M., 2017. Dilatancy in semi-solid steels at high solid fraction. Acta Mater. 125, 187–195. https://doi.org/10.1016/j.actamat.2016.11.066

Lee, S.G., Gokhale, A.M., 2006. Formation of gas induced shrinkage porosity in Mg-alloy high-pressure die-castings. Scr. Mater. 55, 387–390. https://doi.org/10.1016/j.scriptamat.2006.04.040

Li, X., Guo, Z., Xiong, S., 2017. Influence of melt flow on the formation of defect band in high pressure die casting of AZ91D magnesium alloy. Mater. Charact. 129, 344–352. https://doi.org/10.1016/j.matchar.2017.05.009

Li, X., Xiong, S.M., Guo, Z., 2016. Correlation between Porosity and Fracture Mechanism in High Pressure Die Casting of AM60B Alloy. J. Mater. Sci. Technol. 32, 54–61. https://doi.org/10.1016/j.jmst.2015.10.002

Martin, C.L., Favier, D., Suéry, M., 1997. Viscoplastic behaviour of porous metallic materials saturated with liquid Part I: Constitutive equations. Int. J. Plast. 13, 215–235. https://doi.org/10.1016/S0749-6419(97)00009-0

Otarawanna, S., Laukli, H.I., Gourlay, C.M., Dahle, A.K., 2010. Feeding mechanisms in high-pressure die castings. Metall. Mater. Trans. A Phys. Metall. Mater. Sci. 41, 1836–1846.

https://doi.org/10.1007/s11661-010-0222-6

Outmani, I., Fouilland-Paille, L., Isselin, J., El Mansori, M., 2017. Effect of Si, Cu and processing parameters on Al-Si-Cu HPDC castings. J. Mater. Process. Technol. 249, 559–569. https://doi.org/10.1016/j.jmatprotec.2017.06.043

Schindelin, J., Arganda-Carreras, I., Frise, E., Kaynig, V., Longair, M., Pietzsch, T., Preibisch, S., Rueden, C., Saalfeld, S., Schmid, B., Tinevez, J.Y., White, D.J., Hartenstein, V., Eliceiri, K., Tomancak, P., Cardona, A., 2012. Fiji: An open-source platform for biological-image analysis. Nat. Methods 9, 676–682. https://doi.org/10.1038/nmeth.2019

Sistaninia, M., Terzi, S., Phillion, A.B., Drezet, J.M., Rappaz, M., 2013. 3-D granular modeling and in situ X-ray tomographic imaging: A comparative study of hot tearing formation and semi-solid deformation in Al-Cu alloys. Acta Mater. 61, 3831–3841. https://doi.org/10.1016/j.actamat.2013.03.021

Su, T.C., O'Sullivan, C., Nagira, T., Yasuda, H., Gourlay, C.M., 2019. Semi-solid deformation of Al-Cu alloys: A quantitative comparison between real-time imaging and coupled LBM-DEM simulations. Acta Mater. 163, 208–225. https://doi.org/10.1016/j.actamat.2018.10.006

Su, T.C., O'Sullivan, C., Yasuda, H., Gourlay, C.M., 2020. Rheological transitions in semi-solid alloys: In-situ imaging and LBM-DEM simulations. Acta Mater. 191, 24–42. https://doi.org/10.1016/j.actamat.2020.03.011

Sun, S., Hu, Q., Lu, W., Ding, Z., Xia, M., Li, J., 2018. In Situ Observation on Bubble Behavior of Solidifying Al-Ni Alloy Under the Interference of Intermetallic Compounds. Metall. Mater. Trans. A. https://doi.org/10.1007/s11661-018-4818-6

Tzimas, E., Zavaliangos, A., 1999. Mechanical behavior of alloys with equiaxed microstructure in the semisolid state at high solid content. Acta Mater. 47, 517–528. https://doi.org/10.1016/S1359-6454(98)00356-5

Yu, W., Ma, C., Ma, Y., Xiong, S., 2021. Correlation of 3D defect-band morphologies and mechanical properties in high pressure die casting magnesium alloy. J. Mater. Process. Technol. 288, 116853. https://doi.org/10.1016/j.jmatprotec.2020.116853

Zavaliangos, A., 1998. Modeling of the mechanical behavior of semisolid metallic alloys at high volume fractions of solid. Int. J. Mech. Sci. 40, 1029–1041. https://doi.org/10.1016/S0020-7403(98)00011-3

Figure captions

Fig.1. Experimental setup used in I13-2 beamline: (a) Cross-sectional view and side view of the assembly showing the main components of the sample holder (b) Sample holder stage and the Laura PID resistance furnace mounted on the P2R mechanical rig.

Fig.2. X-ray radiographical image sequence showing the injection process (t_0 is at the beginning of loading): (a-d) The injection process from t_0 to t_0 +60 seconds. Note that darker grey indicates the inter-dendritic liquid (Cu-rich), medium grey represents the solid dendritic networks. (See Supplementary Video 1); (e-g) Zoomed-in images show the evolution of the intergranular shear band forming during the injection.

Fig.3. Analysis of radiographic X-ray images using DIC: Processed images showing the local dendrite network distribution change from 33.8 s to 39.8 s after deformation are shown on the left of each panel, and (a-c) corresponding shear strain; (e-f) Horizontal strain; (g-i) Vertical strain evolution are on the right side.

Fig.4. Radiographs capturing the gas bubble behaviour: (a-c) Magnified figures showing bubble growth in the dilation region (see Supplementary Video 2); (d) DIC measurement indicating the localised strain in: I dilation region, II contraction region and III transition region, which is characterised by least deformation; (e)-(g) Enlarged figure indicating a cluster of gas bubbles migrating from high-pressure region to low-pressure region (Supplementary Video 3).

Fig.5. A schematic of mechanism illustrating the strain evolution in the region under high shear strain and the region under compression leading to liquid and solid redistribution.

Fig.6. Quantification of porosity and accumulated volumetric strain at different heights along the injection path: (a) Variation in shrinkage and gas porosity along with the volumetric strain corresponding to the six zones outlined in the inset; (b) A linear correlation between the volumetric strain and percentage of porosity was observed in the six zones, clearly indicating that dilated shear bands are likely to have porosity in castings.